In situ Atomic Level Dynamics of Heterogeneous Nucleation of Graphene From Inorganic Nanoparticle Seeds

Chuncheng Gong[1+], Kuang He[1+], Gun-Do Lee[2], Qu Chen[1], Alex W. Robertson[1], Euijoon Yoon[2], Suklyun Hong[3], Jamie H. Warner[1*]*

[1]Department of Materials, University of Oxford, Parks Road, Oxford, OX1 3PH, United Kingdom

[2]Department of Materials Science and Engineering, Seoul National University, Seoul, 151-742, Korea

[3]Department of Physics and Graphene Research Institute, Sejong University, Seoul, 143-747, Korea

Email: *Jamie.warner@materials.ox.ac.uk; gdlee@snu.ac.kr

+These authors contributed equally to this work

ABSTRACT

An *in situ* heating holder inside an aberration-corrected transmission electron microscope (AC-TEM) was used to investigate the real-time atomic level dynamics associated with heterogeneous nucleation of graphene from Au nanoparticle seeds. Heating monolayer graphene to an elevated temperature of 800 ^{o}C resulted in the removal of the majority of amorphous carbon adsorbates to leave a clean surface and also the aggregation of Au impurity atoms into nanoparticle clusters that were bound to the monolayer graphene. These Au nanoparticles residing on the surface of monolayer graphene cause inhomogeneous nucleation of secondary graphene layers from carbon feedstock present within the microscope chamber. The growth mechanism is found to consist of alternating processes of C cluster attachment and indentation filling to maintain a uniform growth front of low energy. In several cases we observe small back-folded

edge sections of the graphene that can grow in reverse direction before finally flipping over and reattaching to the surrounding region. The secondary layer domains start as highly polycrystalline, but evolve with time into better crystallinity. Tight-binding molecular dynamics (TBMD) simulations are used to understand the detailed lowest energy step-by-step pathways associated with GB migration and crystallization processes. We find the motion of the GB is discontinuous and mediated by both bond rotation and atom evaporation, supported by density functional theory calculations and TBMD. These results provide insights into the formation of crystalline seed domains that are generated during bottom-up graphene synthesis.

KEYWORDS: AC-TEM, graphene, GB, *in situ* TEM, crystallization, grain growth.

Chemical vapor deposition (CVD) of graphene on Cu substrate has been a promising method to synthesize large area graphene with industrial scalability.[1–6] Graphene domains nucleate on the Cu surface and grow larger as precursor feedstock is supplied until they eventually merge together to form a continuous polycrystalline film.[7] The formation of graphene domains can be either from heterogeneous and homogenous nucleation processes. Heterogeneous nucleation involves using seeds, often particles, to lower the precursor concentration threshold for nucleation to occur compared to homogeneous nucleation.[8,9] Understanding these initial nucleation processes of graphene domains is critical for developing new synthetic strategies for CVD growth of high quality graphene continuous films. Previous results have shown that individual graphene domains can be single crystals, but in some cases are polycrystalline.[1,8,10–12] Having polycrystallinity from a single domain region significantly increases the number of grain boundaries (GB) in the final continuous films of graphene as the domains merge together.

The GBs can impact the mechanical[13–18], electrical[19,20,8] and chemical[21] properties of graphene. The atomic structure of dislocations and GBs in graphene has been investigated in both experiment and theoretical calculations, primarily for the potential application in device fabrication and

nanoengineering.[22–32] Early in 1988, Albrecht *et al*. reported the observation of tilted GBs in graphite by scanning tunneling microscope (STM).[33] It was not until many years later that the atomic structure comprised of arrangements of pentagon–heptagon (5–7) edge dislocations was revealed by high resolution transmission electron microscopy (TEM) experiments.[34] Similar results were later achieved by multiple TEM and STM observations.[35–37] The formation of 5–8–5 linear GBs has also been reported in polycrystalline graphene grown on Ni (111) substrate due to the strong graphene-substrate interaction.[38] Experimental studies of the atomic level migration of a GB using an aberration-corrected TEM (AC-TEM) revealed migration mediated by bond rotations, however *ab initio* theoretical calculations indicate that GBs can also migrate by evaporating a carbon dimer.[36,39] After high temperature annealing (600^{o}C), curved and aperiodic GBs in CVD grown graphene reconstruct into straighter and periodic forms.[37] *In situ* experiments within a TEM at high temperatures of 2000 K by Joule heating found carbon adsorbates on monolayer graphene transformed into polycrystalline graphene domains separated by GBs.[40] Reconfiguration of carbon bonds at the GBs was found to give rise to better crystallinity.

Prior work has shown that carbon can attach to preexisting edges of graphene to further continue its growth. Liu *et al.* reported the *in situ* growth of a second-layer graphene inside a AC-TEM from the step edge of an existing domain under beam irradiation.[41–45] The crystallinity and growth rate of the newly grown area were shown to be temperature dependent, with single silicon atoms located at the step edge suggested to act as a catalyst for second layer graphene growth from hydrocarbons.[36] Homogenous nucleation of small graphene seeds are often study by STM and can reveal the transition from molecular disordered cluster to small crystalline fragment of sp^2 carbon.[46] However, there are hardly any atomic level studies related to heterogeneous nucleation of graphene domains from seeds, such as metal nanoparticles.

In this report, we utilize an *in situ* heating holder within an AC-TEM to study the dynamics of heterogeneous nucleation of graphene domains from metal nanoparticles. We study the growth of the graphene domain size in regards to the site-specific addition of carbon atoms and also the GB

transformations that underpin the increase in crystallinity of the domains. The initial graphene was synthesized by ambient pressure CVD method using melted copper on molybdenum substrate as the catalyst as previously reported.[10,47] The graphene sheet was subsequently transferred onto a SiN grid designed for *in situ* high temperature TEM experiments (DENSsolutions). The heating holder allows us to accurately control the specimen temperature from room temperature to 800 ºC and capture detailed real-time dynamics. Au nanoparticles on the surface of graphene are found to act as catalyst sites for the heterogeneous nucleation of secondary layer graphene domains. As the domain size increases and the growth rate reduces, we examine the discontinuous movement of GBs that further drives the growth and coalescence of nanograins in the graphene domain.

Results and discussion

As shown in Figure 1, a monolayer of graphene was heated up to 800˚C inside the TEM using the *in situ* heating holder (Figure 1a), which causes the amorphous carbon surface adsorbates to evaporate and reveal the lattice structure of graphene. This effect has also been described with more detail in previous experiments.[48,49] We selected an area of graphene containing aggregated nanoclusters of heavier atoms, likely to be residuals from the synthesis and transfer process. Energy-dispersive X-ray spectroscopy (EDX) taken on the nanoparticle shows the presence of Au, while the EDX spectrum taken from the pristine graphene area shows no Au signal. Some Si atoms may also be present in the nanoparticle cluster. The Au atoms have a tendency to form clusters on the surface of graphene even though it doesn't constitute a crystallographic structure at temperatures above 600 ºC. The clusters in Figure 1d adhere to the surface of graphene while other hydrocarbon adsorbates evaporate at 800˚C. The Au nanoparticle is surrounded by a small amount of carbon on the surface of graphene. 600˚C was found to be the optimal temperature where hydrocarbons attach to the seed and begin to slowly grow graphene. At 800 ºC, the rate of graphene growth basically reached an equilibrium with the etching of edge atoms and the formation of a secondary layer of graphene is limited.

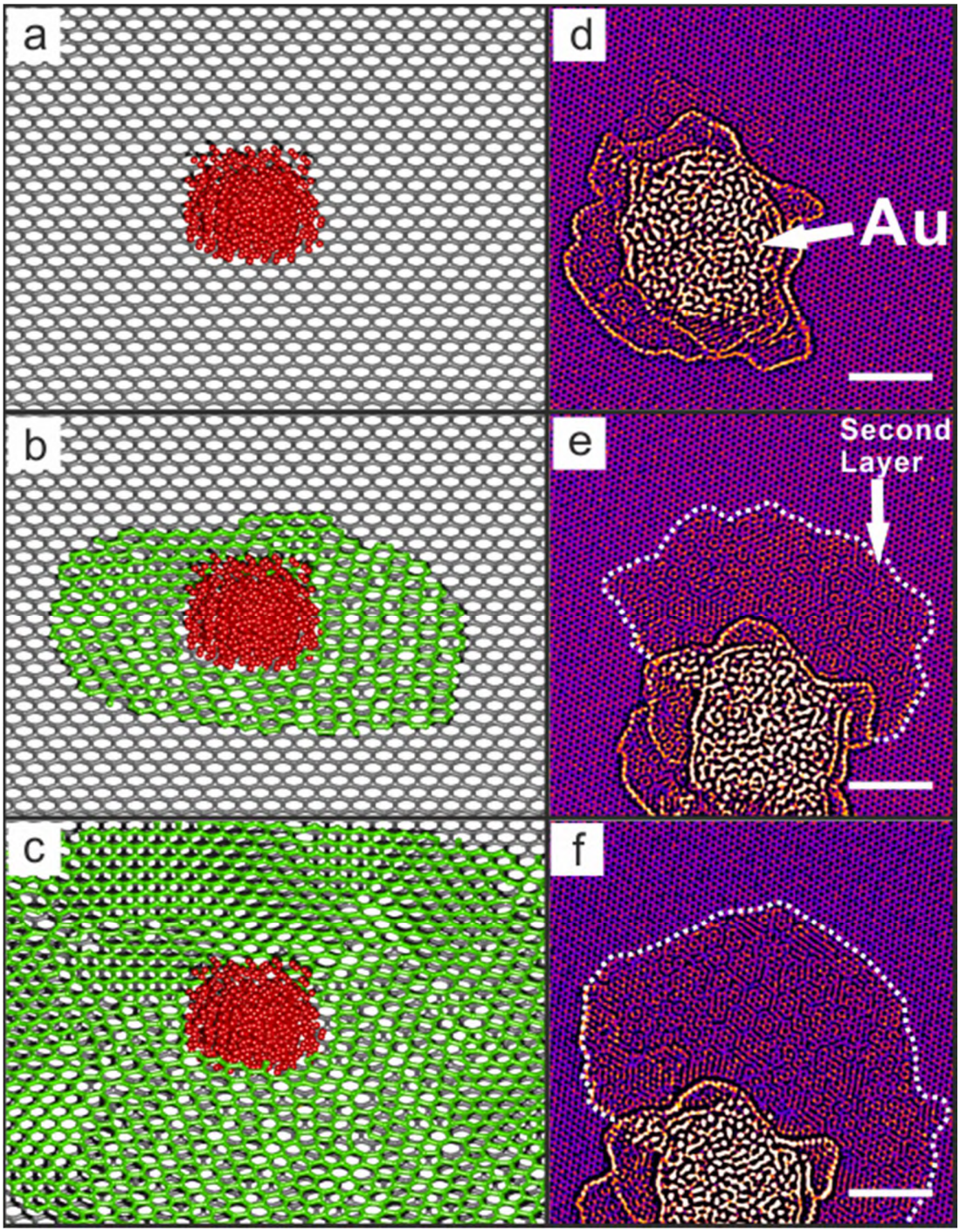

Figure 1. *In situ* heterogeneous nucleation and growth of a secondary layer of graphene around an Au nanoparticle on the surface of monolayer graphene. (a) At 800˚C, the surface contamination evaporates off, leaving only the particle adhere to the surface of graphene. (b) Reducing the temperature down to 600˚C, second layer starts from the Au cluster *via* heterogeneous nucleation. (c) The second layer continues to grow within the area under electron beam irradiation. The results from the experiment designed in (a-c) are shown in (d-f), demonstrating the nucleation and growth process. All scale bars = 3nm.

According to the classical nucleation theory, heterogeneous nucleation is much more commonly observed as oppose to homogeneous nucleation and the reaction process is also much faster due to the lower nucleation energy barrier. In the case of the *in situ* high temperature graphene growth in the AC-TEM, electron beam irradiation of the pristine monolayer graphene area did not lead to the formation of a secondary layer of graphene on top. However, around the Au particles a secondary layer of graphene nucleates swiftly and continues to grow at 600^{o}C. Figure 2a-d shows a time series of secondary layer growth with the underlying monolayer graphene removed from image using a mask filter in the Fourier transform, similar to those shown in figures 4 and 6. The growth rate is shown in figure 2e by plotting the area of the secondary layer with time for all 39 frames over 8 min 41 s. Excluding the odd first point, the results exhibit an excellent linear relationship. The growth rate obtained from the slope of the linear equation is 0.14 nm^2/s. This relatively slow growth rate enables us to study the dynamics of the growth frontier.

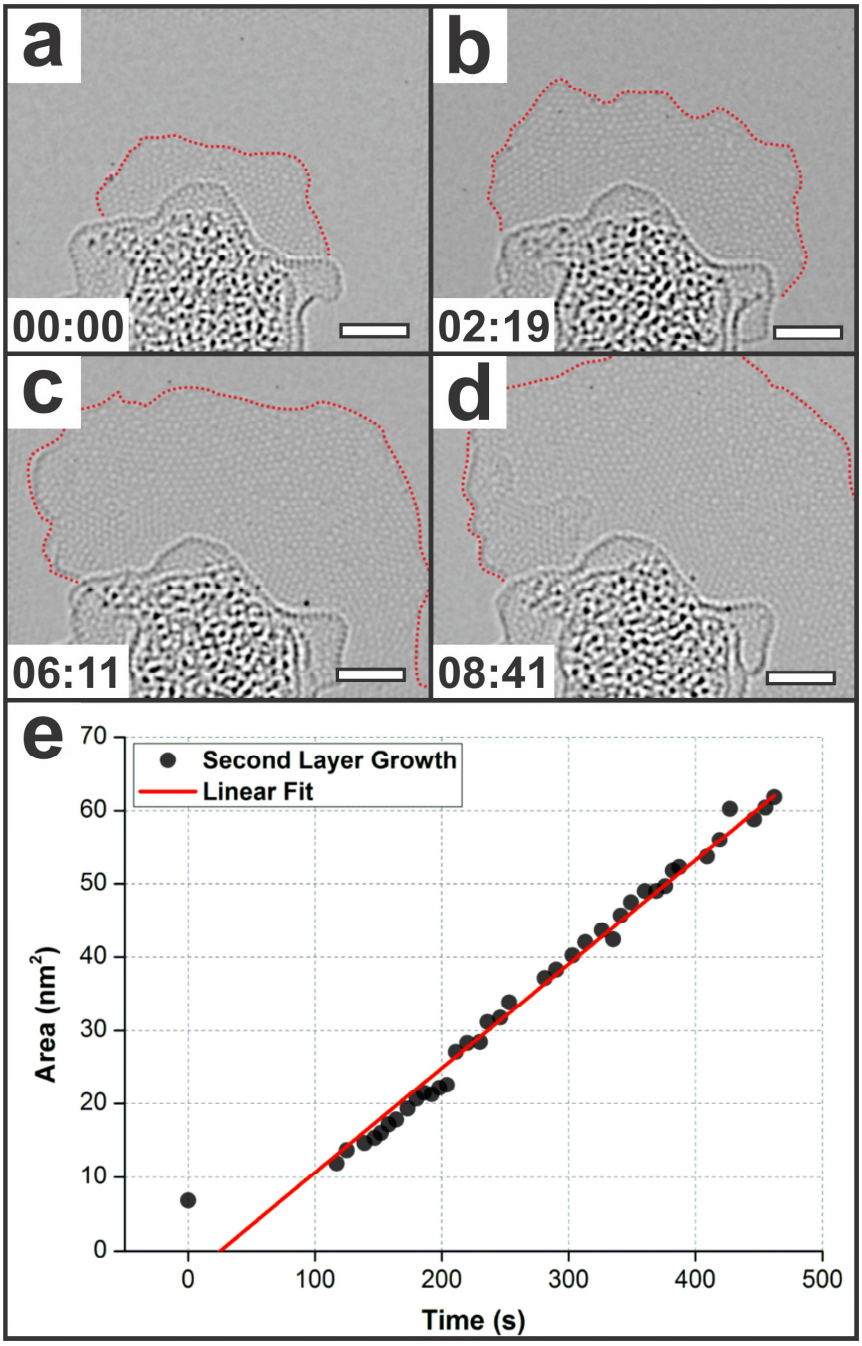

Figure 2. (a)-(d) Time series of AC-TEM images showing the growth of a secondary graphene layer from surface adsorbate attachment. The frontier for the second layer is shown by the red dotted lines. The underlying monolayer graphene has been removed from the images using a filter mask in the Fourier transform. All scale bars = 3nm. (e) The area for the as-grown second layer is plotted against time.

The growth front is carefully studied to gain deeper understanding of how the domain gradually expands its size atom by atom. There is a tendency for the perimeter to adopt a smooth round configuration, shown in Figure 3. For example, in Figure 3(a)-(f), where the time series of AC-TEM

images are examined, a cluster of atoms adds onto the pre-existing graphene to continue the growth process, indicated by the arrow Figure 3b. This leads to the roughening of the edge in this local region and subsequent frames show that further atom cluster deposition fills in around this to smooth the edge back out. This process of 'indentation filling' is highlighted in Figure 3d,f and a second example is presented in figure 3(g)-(l). Our observation agrees with the classical nucleation theory, according to which the newly formed structure that has greater surface area and is therefore not energetically favored. Instead of growing uniformly in all directions by single atom attachment at all edge sites, a cluster of carbon atoms firstly attach to one edge location. The initial seed formed in both cases in figure 3 are not well crystallized and show lots of non-hexagonal rings indicative of amorphous 2D carbon or highly defective graphene.

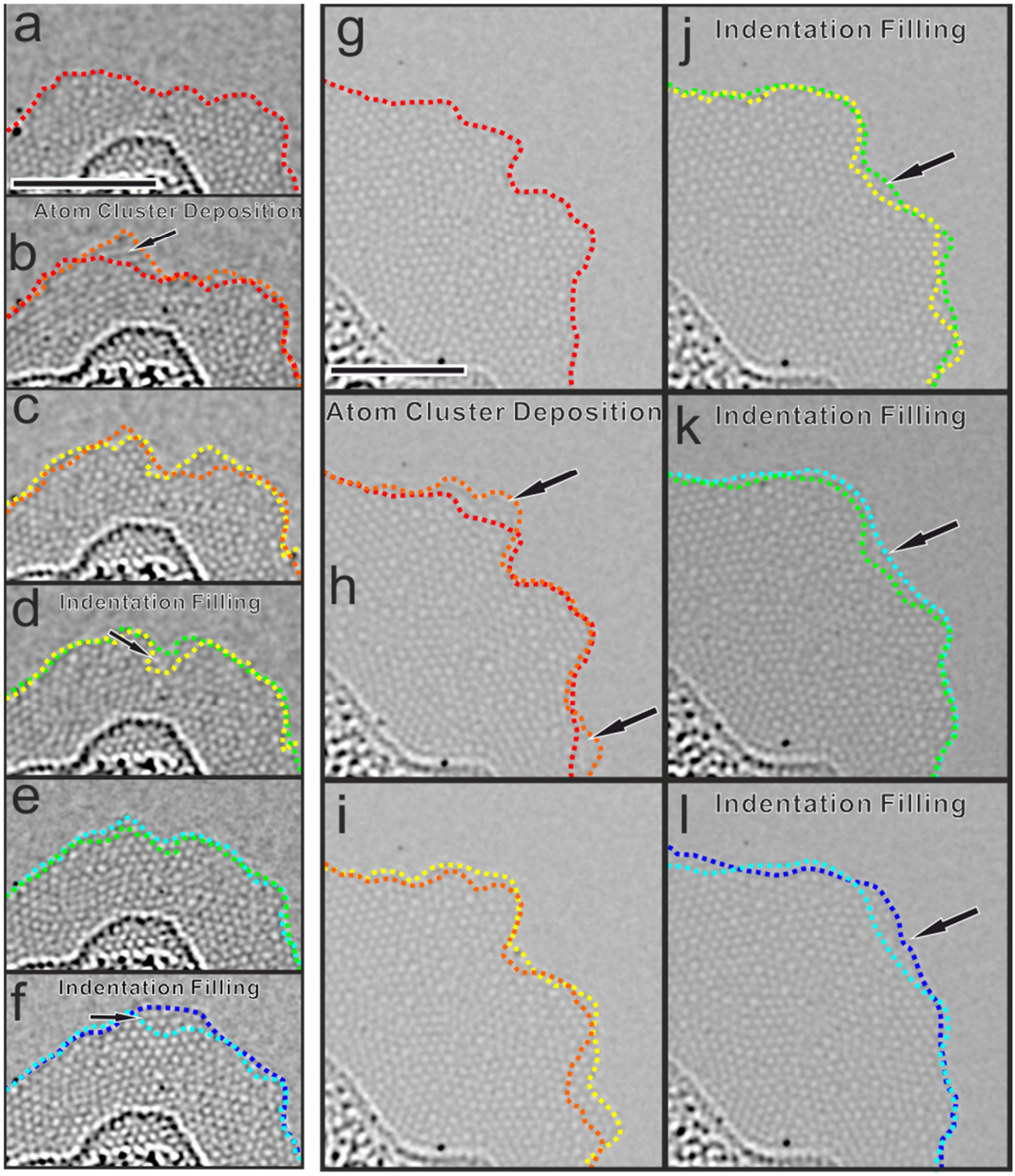

Figure 3. Two different examples, (a-f) and (g-l), showing in-situ atomic level dynamics of the graphene edge growth. The time series of AC-TEM images show the cluster addition of C atoms to the edges of amorphous graphene domains. Time between frames is ~10 s. The perimeters are color coded differently to allow visual comparison between the two consecutive frames. All scale bars = 3 nm. The underlying monolayer graphene has been removed by a filter mask in the Fourier transform.

In some circumstances the edge of the secondary graphene domain showed increased contrast due to back-folding compared to other edge regions, figure 4. We increased the temperature from 600^{o}C to 800^{o}C to slow down the growth rate so that we could investigate the atomic configuration of the edges and also the crystallization from amorphous to sp^2. Figure 4a is the side view of an atomic model of a back-folded secondary layer of graphene, with corresponding multislice image simulations shown in figure 4b. A red dashed line in figure 4b indicates the back-folded region. It is apparent that the contrast along the folding pleat increases dramatically. In order to quantify this, an image is reconstructed from the FFT using an exclusion mask for the set of hexagonal spots associated with the underlying graphene, (inset in Figure 4c). A boxed line profile, Figure 4f, was taken from the black rectangle highlighted region along the direction shown with a black arrow in Figure 4c. Figure 4d shows an AC-TEM image of a region of secondary layer graphene, whose presence is evident from the Moiré pattern. The reconstructed image in Figure 4e excludes the signal from the bottom graphene layer, leaving only secondary layer graphene for analysis. A boxed line profile figure is also taken from the black boxed region along the arrowed direction, and the result is presented in Figure 4g. The red dashed box highlights the region with apparent enhanced contrast, accordant with what is observed in the multislice image simulation in Figure 4f. As have been previously reported,[50,51] the increase in contrast originates from multiple atoms under the projection of electron beam along back-fold. However, it is difficult to determine whether the secondary layer of graphene is folded back or just bonded to the first graphene layer, as both introduce an increase in contrast (Figure S2).

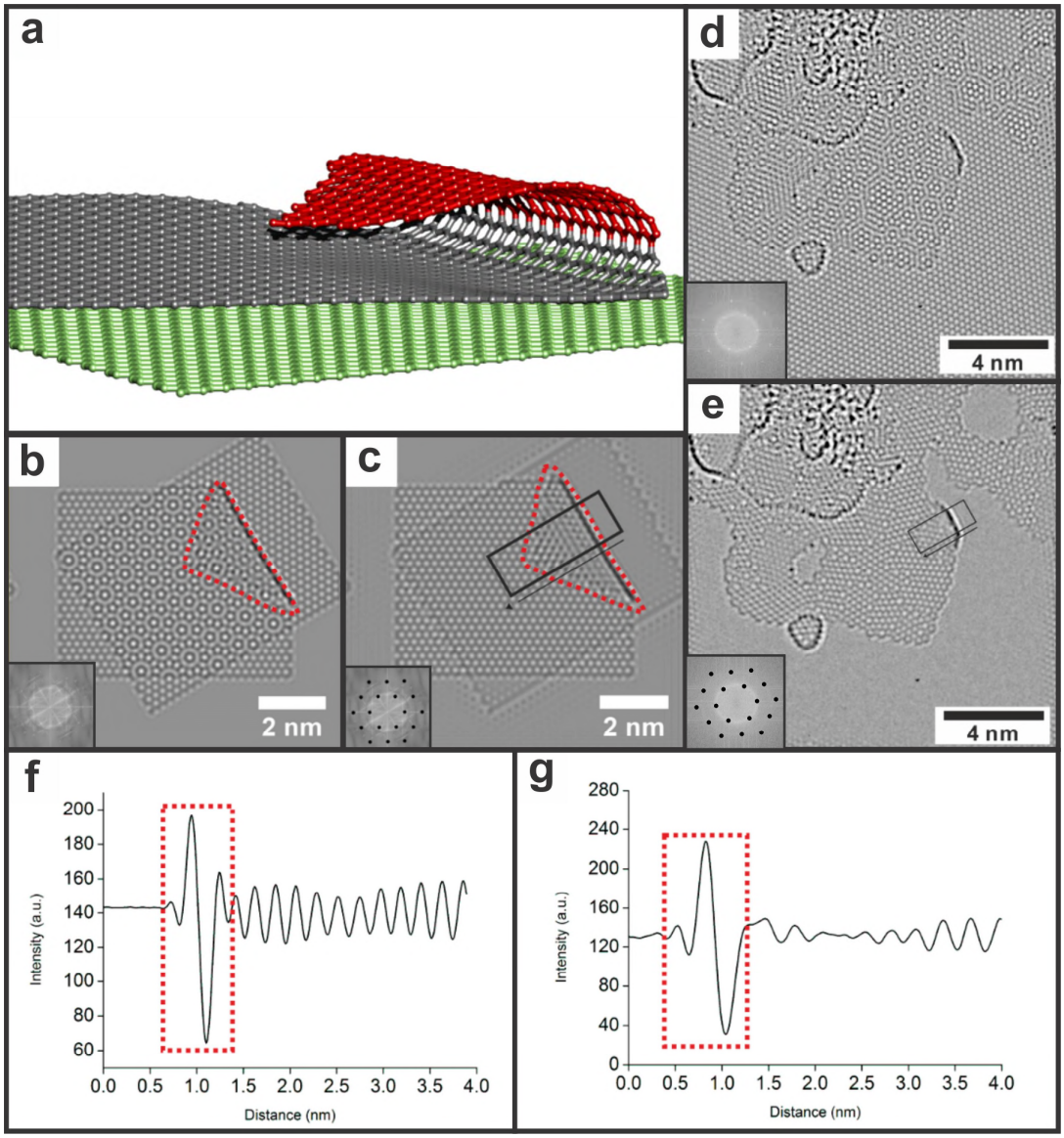

Figure 4. Back-folding of the secondary layer of graphene. (a) Schematic illustration of the secondary layer of graphene being folded back. (b) the multi-slice image simulation of the atomic model in (a) with the inset showing the FFT of the simulated image. (c) Reconstructed images from the FFT negative mask, shown in the respective inset. (d) An AC-TEM image of bilayer graphene with folded edge. (e) Reconstructed image from the FFT negative mask in the respective inset. (f) and (h) are intensity profiles taken from the boxed regions in (c) and (e) along the arrow indicated directions.

Studying the dynamics of the back folded region of the secondary layer of graphene provides further insights into the structure. Figure 5a-d are time series of AC-TEM images with red dashed lines highlighting the frontier of the secondary layer and shown in the inset. Figure 5e-h are reconstructed images from the negative masked FFT shown in the insets. Red rectangles highlight the areas of interest, which are magnified and shown in Figure 5i-l respectively. Figure 5i shows a dark contrast line that was

previously discussed originating from back-folding or possibly bonding to the bottom layer. In this time series study, we could see the darker contrast along the edge in Figure 5(j) fades away in the subsequent two frames (Figure 5(k) and (l)), an area of extra graphene extends out where used to be the darker contrasted boarder over the course of just 10 seconds. This indicates the extra area came from the unfolding of the folded area. The red dashed line in Figure 5(k) highlights the extra region formed in the unfolding process. Figure 5(m)-(p) demonstrates this process with atomistic models: with figure 5(m) showing the folded model and figure 5(n) showing the structure after unfolding. Figures 5(o) and 5(p) are side views of the two models respectively. This study of the edge dynamics of the secondary layer of graphene confirms the darker contrast arises from back-folding rather than edge bonding.

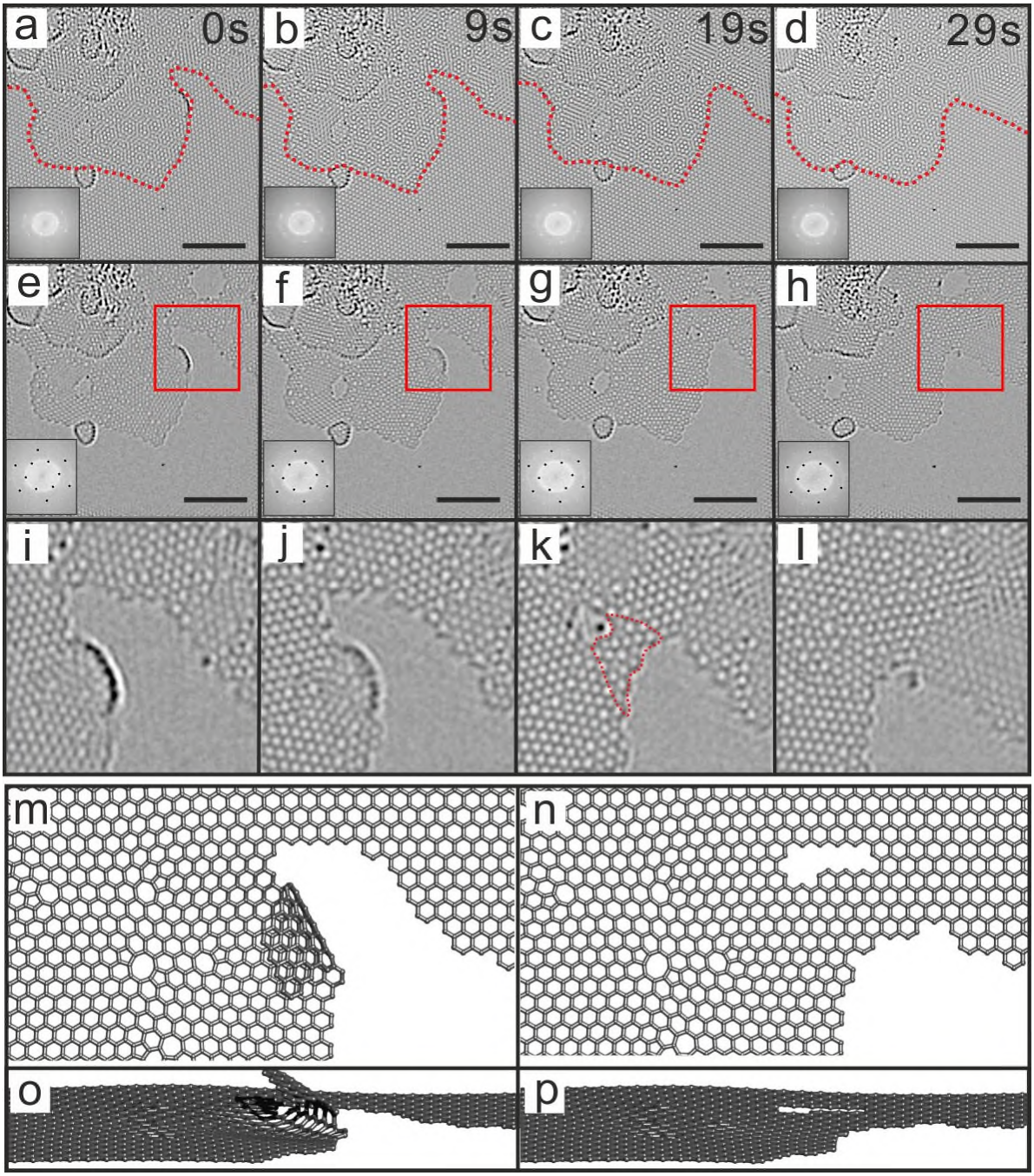

Figure 5. Dynamics of an unfolding graphene layer at 800˚C. (a-d) Time series of AC-TEM images showing a secondary layer of graphene initially grown at 600˚C and then examined at 800ºC. The FFTs are shown in the respective insets. (e-h) Reconstructed images from the FFT negative mask shown in the respective insets. (i-l) Magnified AC-TEM images taken from the red boxed regions in (e-h) to highlight the unfolding dynamics. (m-p) Front and side views of the atomic models before and after unfolding. All scale bars = 4 nm.

The small graphene domains begin to crystallize at high temperatures to achieve improved sp^2 ordering and figure 6 shows this in detail for the elevated temperature of 800 ºC. Our data set in total consists of

72 AC-TEM images taken over 34 min 07 s. Figure 6a shows the same image as Figure 5a but in higher magnification in order to examine the atomic scale lattice configuration. The image is then filtered using a mask in the FFT to eliminate the underlying monolayer graphene and reconstructed (Figure 6b), then maximum filtered (Figure 6c) for better visualization of non-hexagonal rings. Yellow circles in Figure 6b highlight heavier atoms (probably Au) trapped in graphene and at the edge. Unlike previous reports, the newly formed graphene in our experiment is neither fully crystalline nor purely amorphous. In Figure 6d the crystalline area in the image is shaded with color and the non-hexagonal rings are marked by the dashed polygons. It is apparent that a large proportion of the top layer is comprised of well crystallized graphene grains. However, the lattice orientation of each grain is randomly distributed and the grain size is in the nano scale, from 1 to 2 nm. There is also a large amount of pentagons and heptagons and several octagons at the boundary of the grains. The majority of the GBs can be regarded as highly aperiodic and curved 5–7 dislocation strings. This result is similar to the TEM images taken by Westenfelder *et al.* at 1000 K for graphene transformed from amorphous carbon.[40]

As reported in our previous work, both glide and climb motions for dislocation in graphene can be significantly accelerated at temperatures above 500 ^{o}C under 80 kV electron irradiation.[52] Therefore, as expected, we observed subsequent migration of GBs and crystallization of nano-sized grains over time. Figure 6d–i shows a time series of AC-TEM images of the crystallization with the images processed the same way as Figure 6c. A dozen graphene grains have merged into 3 larger ones with sizes of 2–5 nm in the first 11 minutes. Sinuous GBs with high curvature tend to reconstruct into a more symmetric and straight shape over the whole time period. The growth rates for the domains shaded in green and cyan are plotted in Figure 6j as the form of the number of undistorted hexagons within the domain versus time. The growth process for both grains is discontinuous. Take the grain shaded in green for example, despite the apparent shape reconfiguration of GBs in the first 4 min (Figure 6d and 6e), the grain size does not change much (Stage 1, T1). A sudden change in the grain size took place between 4–9 min by consuming smaller grains colored in purple and yellow (Stage 2, T2). No more grain merging is observed afterwards but the movement of GBs continues at a much slower rate, leading to the gradual shrinkage of grain size

in the next 19 min (Stage 3, T3). The evolution of the cyan grain is similar. The statistics in Figure 6k shows that significant reduction in non-hexagonal rings occurs between 6 min 1 s and 7 min 22 s, approximately the same period when the coalescence took place.

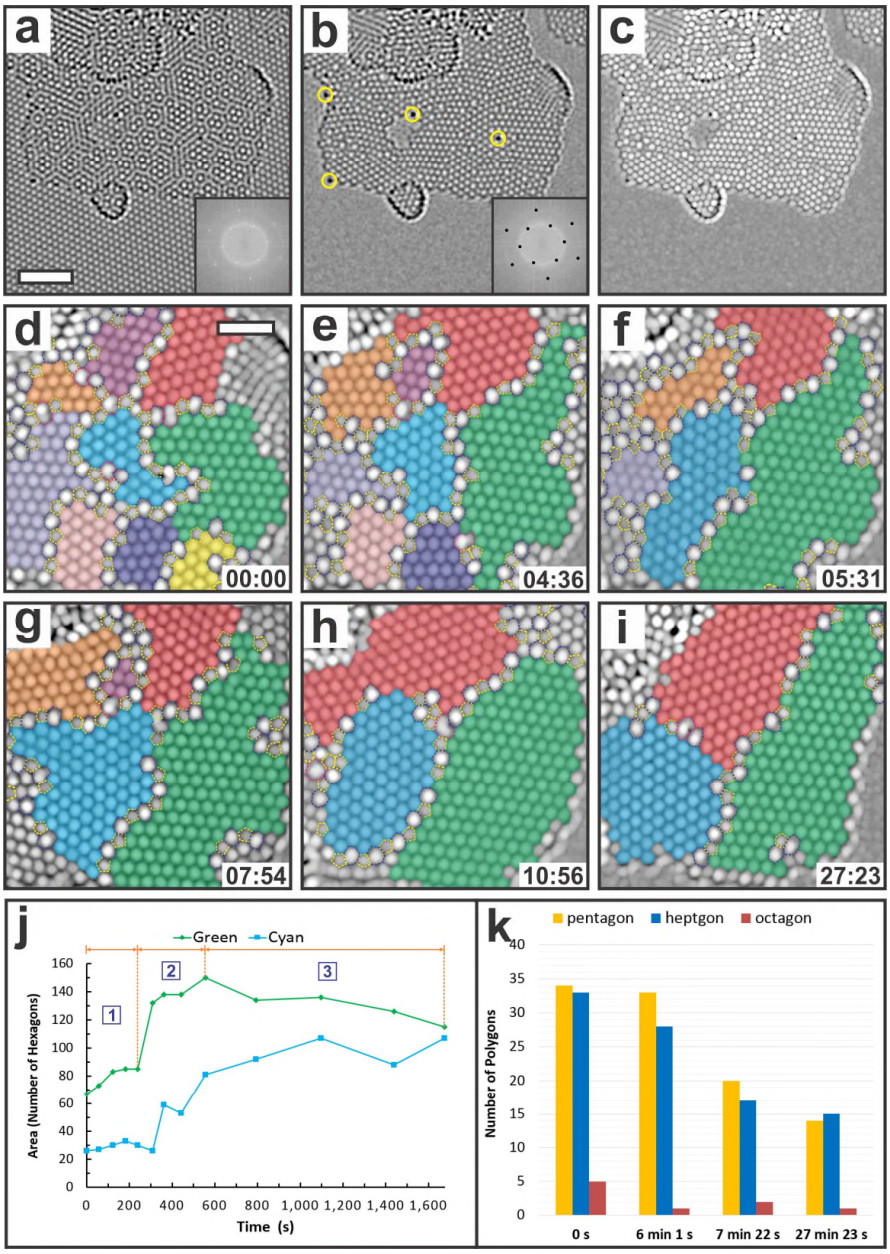

Figure 6. Crystallization of the as-grown graphene layer over time at 800 ºC. (a–c) Image processing details. (a) is cropped from Figure 5a and then magnified with the inset showing its fast Fourier transform (FFT). (b) Reconstructed image from FFT negative mask shown in the inset showing the top graphene layer. (c) Maximum filtered image of (b). (d–i) Six time series frames showing the growth and coalescence of graphene grains, overlaid with false colors. The pentagon, heptagon and octagon in the GBs are indicated by the dashed yellow, blue and pink polygons, respectively. (j) Two trend lines representing the size

change of the grains shade in blue and cyan as a function of time. (k) Statistics of non-hexagonal rings in the GBs. Topological defects within the grain or at the edge are not included. The scale bar in panel a and panel d is 2 nm and 1 nm, respectively.

In Figure 7, we examine the coalescence of grains colored in cyan and pink in Figure 6e at the atomic level. The structural change between Figure 7(a) and (b) is accomplished by three sequential SW bond rotations within 22 s as schematically illustrated in the atomic models shown in Figure 7(e)–(h). Insights into the sequential order is provided by high temperature tight-binding molecular dynamics (TBMD) simulations (Movie 1). We find that the bond rotations are initiated at the junction of three highly curved GBs, where there is a high density of non-hexagonal rings (Figure 7(a),(c) and (e)). It has been shown that bond rotation and atom loss are more likely to occur in the defective area under electron beam irradiation due to a lower sputtering cross section.[28] Our recent work also shows such a phenomenon becomes more pronounced at elevated temperatures.[52] In Figure 7(i), we calculated the energy barriers for all three rotations using density functional theory (DFT) which are 4.57, 5.03 and 4.81 eV respectively, all significantly lower than the energy required to form a SW defect (9–10 eV) or dislocation glide (6.95 eV).[52–54] The energy for each bond rotation to reverse back is more than 3 eV higher. This explains why the GBs unwound so rapidly in T2, and that the temporal resolution of our imaging was insufficient to capture any intermediate structure. As a consequence of the structural reconfiguration in Figure 7(a)–(h), the total energy of the second layer graphene is decreased by 9.21 eV with the curvature of GBs greatly reduced, as shown in Figure 7(b),(d) and (h), which is in agreement with previous research indicating that the driving force for GB migration energetically favors decreasing GB length and curvature.[36] Another similar example is given in Figure S3 where 10 bonds rotate in a time span of 13 s leading to the incorporation of a small graphene grain into a larger one.

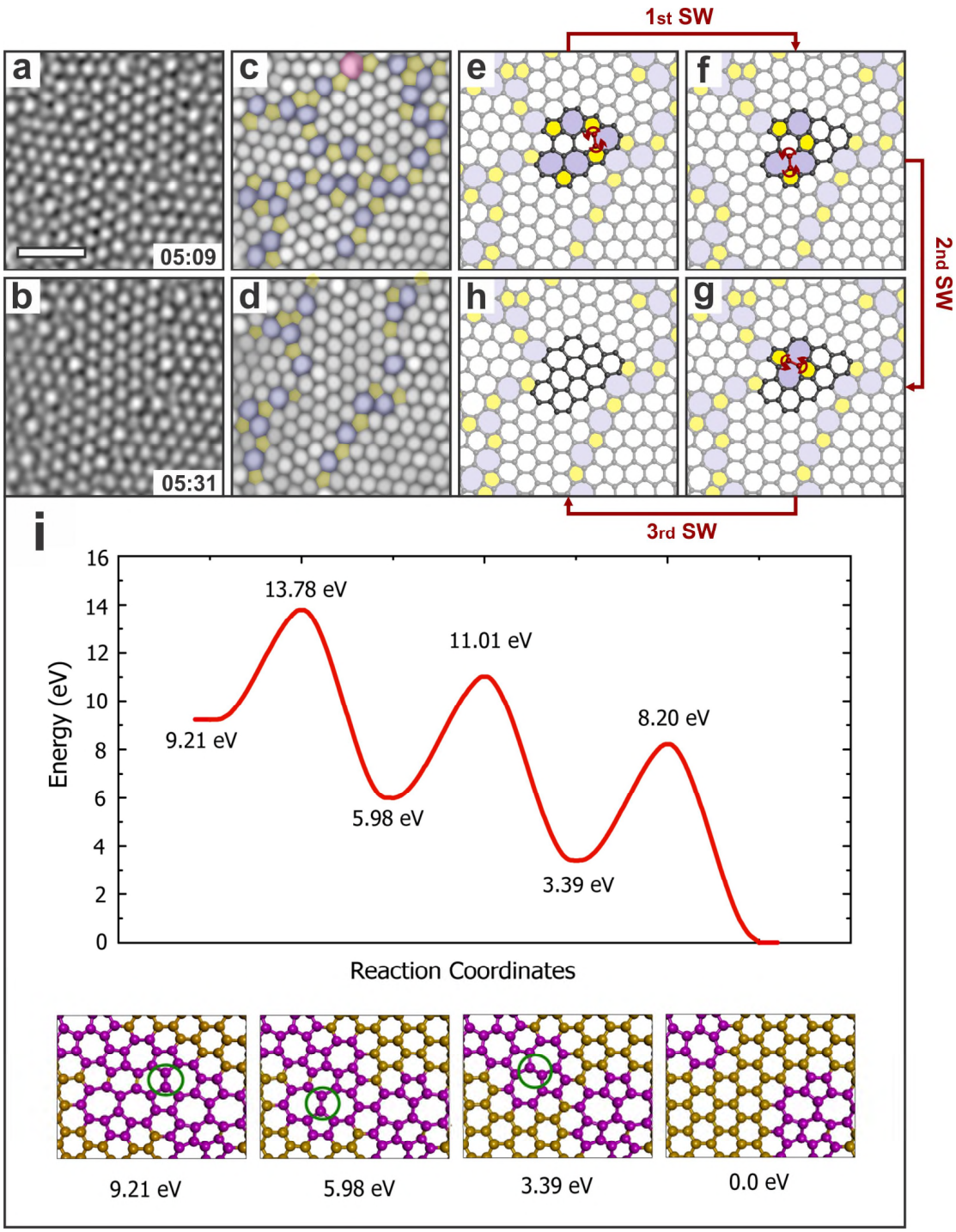

Figure 7. The merging of two grains *via* three bond rotations. (a,b) FFT reconstructed AC-TEM images showing the atomic structure of the second layer graphene at 5 min 9 s and 22 s later. (c,d) Maximum filtered images calculated from (a,b) with non-hexagonal rings shaded in color. (e,h) Atomic models corresponding to (a) and (b). (e–h) A probable pathway for the detailed structural change between the GBs in (a) and (b) suggested by high temperature tight-binding molecular dynamics (TBMD) simulations. The arrows and atoms highlighted in red indicate the bond undergoes a SW bond rotation in the next panel. The color scheme in the maximum filtered images and atomic models represent the number of carbon atoms in each

ring, with 5 = yellow and 7 = blue. (i) Density functional theory (DFT) calculated energy barrier for the pathway shown in (e–h). The scale bar in panel a is 1 nm.

Figure 8 shows how dislocation movement can play an important role in grain merging at the edge regions. The grains to be merged are the ones shaded in blue and green in Figure 6(d). A carbon dimer was removed from the GB after 16 s, resulting in the 5–8–5–5–7 defect at the boundary reconfiguring into a 5–7 edge dislocation and the 5^{o} angle mismatch in Figure 4(a) partly compensated (Figure 8b). The GB totally annihilates after another 17 s (Figure 8(c)). The individual steps for this transformation were not resolvable in our imaging conditions. Figure 8(h)–(k) shows a plausible pathway by forming an isolated dislocation core at the first instance (Figure 8(i)). The dislocation then disappears by gliding towards the edge along its glide plane (indicated by the red arrow in Figure 8(i)) making the lattice mismatch eventually compensated. Recent work investigating the interactions between dislocations and graphene edges has shown it is energetically favorable for a dislocation to glide towards the edge of graphene, provided the distance is close enough.[55] The structural change between Figure 8(j) and 8(k) were accomplished by two further bond rotations. Evidence to support this is highlighted in Figures 8(a) and 8(c). Two rows of zigzag-oriented graphene lattice are colored in cyan and orange in Figure 8(a) for visual reference. They change into one zigzag row in Figure 8(c), which can only result from the slip behavior of an edge dislocation.

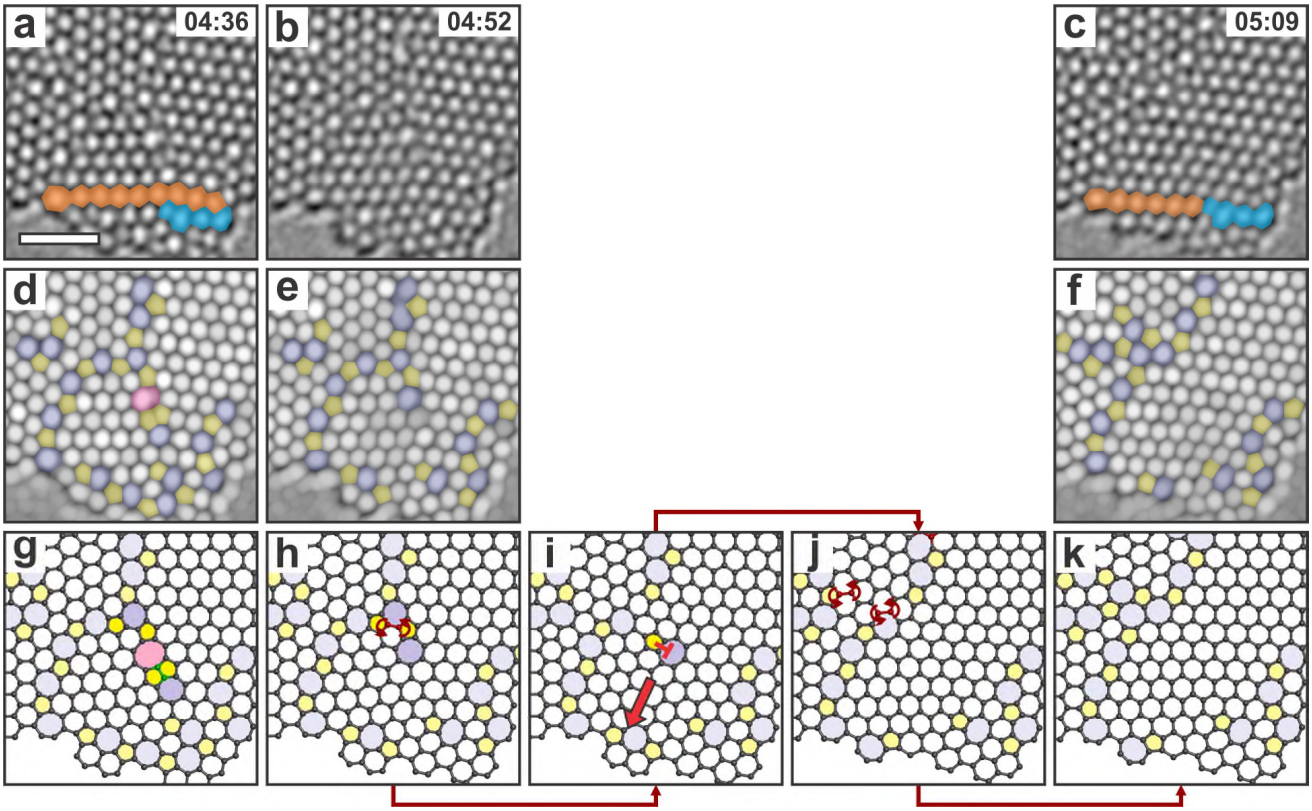

Figure 8. The coalescence of two grains *via* the slip of an edge dislocation towards the edge. (a) FFT reconstructed image of the second layer graphene at 4 min 36 s, which loses a carbon dimer at GB in the next frame, shown in (b). (c) A following image showing annihilation of GB and merging of two grains at graphene edge. (d–f) Maximum filtered images of (a–c). (g,h,k) Atomic models of (a–c). (h–k) A possible path for the structural reconfiguration between panel b and c. A SW rotation firstly transforms the GB into an isolated pentagon–heptagon configured dislocation (i), which subsequently disappears by gliding to the edge. Bonds that undergo a SW rotation in the next frame are highlighted in red and by arrows. Atoms to be sputtered are highlighted in green. The color scheme in the maximum filtered images and atomic models represent the number of carbon atoms in each ring, with 5 = yellow, 7 = blue and 8 = pink. The scale bar in panel a is 1 nm.

After the first 11 min, the original nano-sized grains merged to form three larger ones (colored in cyan, red and green in Figure 6(h)). Instead of combining into an even larger grain, only occasional bond rotation and atom loss occurred in or near the GBs over the next 17 min (Figure 9), similar to the basic glide and climb step of a 5–7 dislocation core.[27] The relatively slow migration rate enables us to trace the structural change of the second layer atom by atom between each frame. In Figure 10, we observed the intermediate structure before a carbon dimer was completely sputtered from GB. The defect structure in Figure 10(a) remained stable for 35 s, before a carbon atom acquired enough energy in an electron

collision to break two sp^2 bonds and rotate perpendicular to the graphene plane (Figure 10(b)). The magnified view and its corresponding multislice simulated TEM image on top of Figure 10(b) show that the vertically stacked carbon dimer has a higher intensity than other carbon atoms. The dimer was at last removed out of the graphene plane in another 32 s. In Figure 11, we compare the energy barriers of two mechanisms to evaporate a carbon dimer. The flipping of the dimer firstly needs to overcome a barrier of 9.26 eV. The vertically stacked structure is surprising stable with the energy only 2.41 eV higher than ground state suggested by DFT calculation. The energy barriers to further evaporate the vertically stacked dimer are 2.75 and 2.2 eV respectively. Theoretically the two atoms may also be sputtered one after another but the energy required for this process is far higher (12.7 eV). Movie 2 shows the dynamic process simulated by high temperature TBMD.

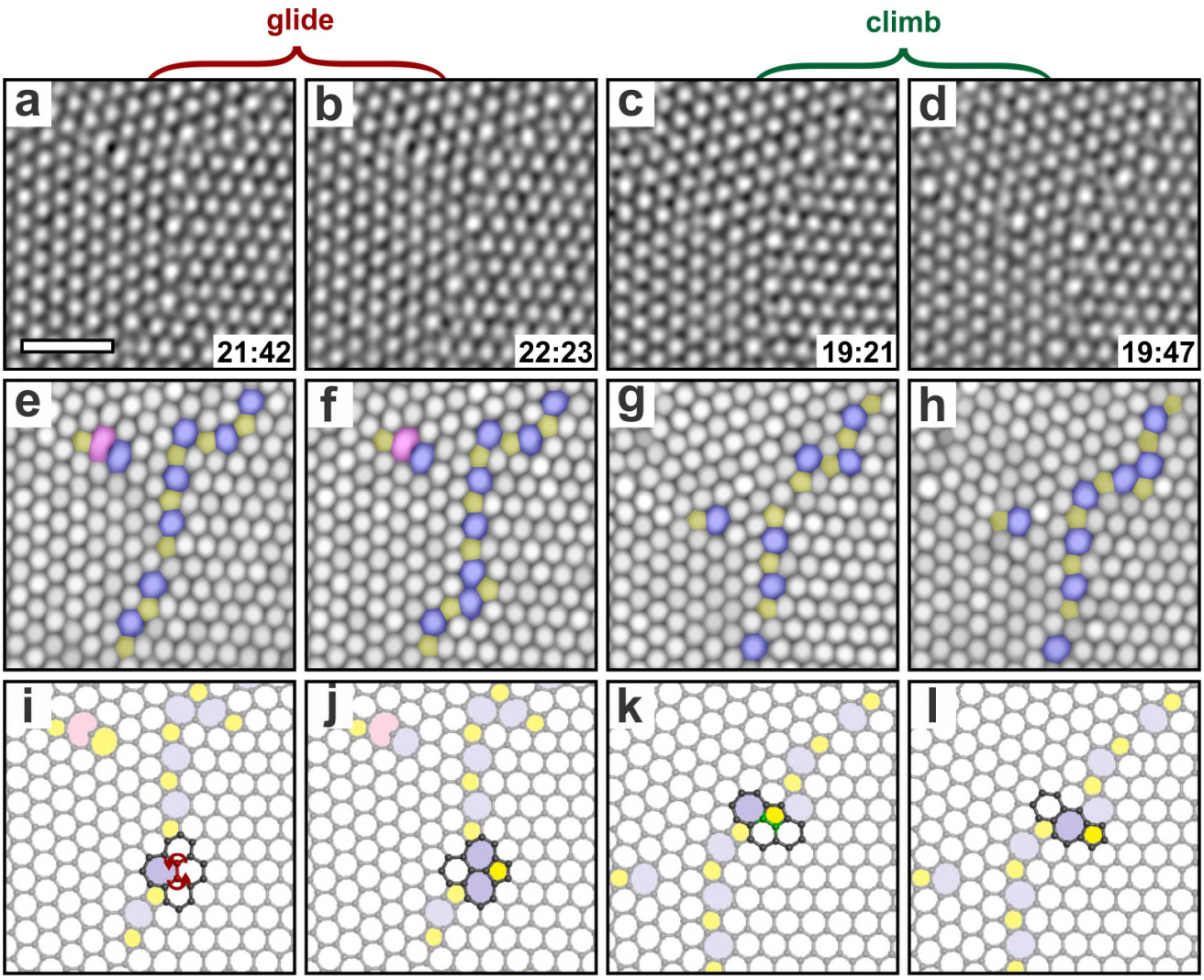

Figure 9. Glide and climb motions of a 5–7 dislocation within the GB. (a, b) AC-TEM images showing a basic glide step. (c, d) AC-TEM images of a basic climb step accomplished by sputtering a carbon dimer. (e–h) Maximum filtered images. (i–l) Atomic models. The scale bar in panel a is 1 nm.

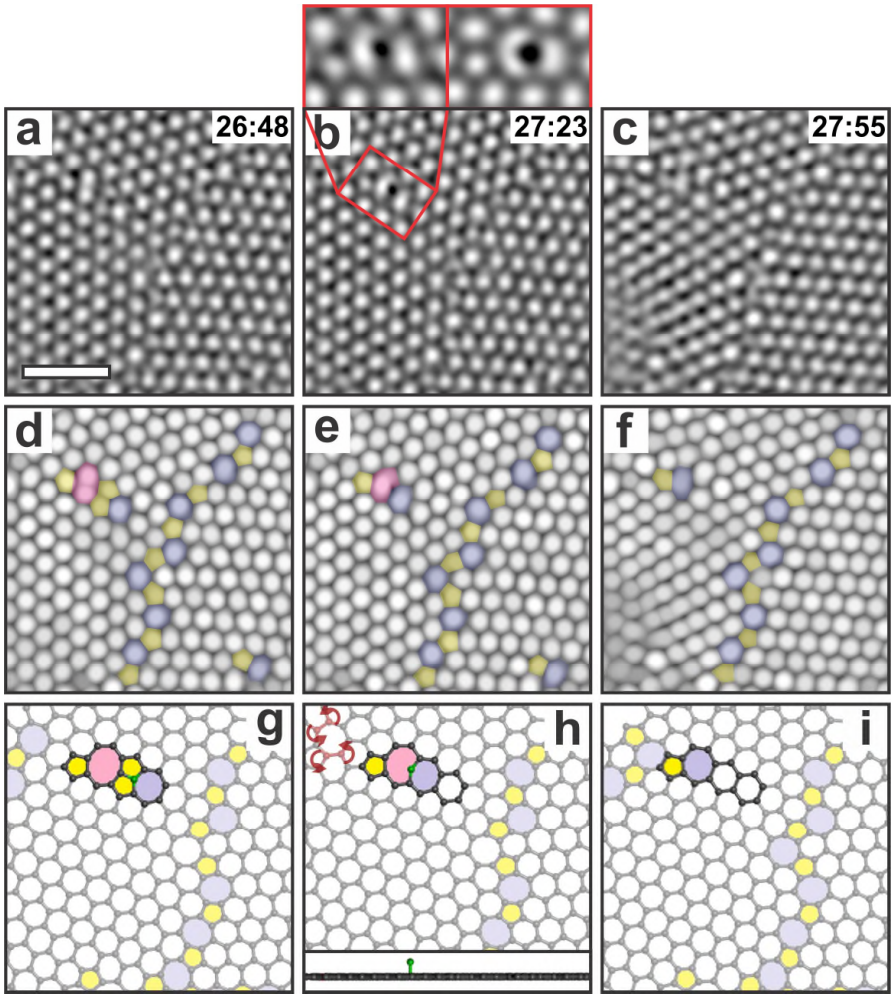

Figure 10. Evaporation of a carbon dimer in the GB. (a) FFT reconstructed AC-TEM images of the second layer graphene at 26 min 48 s. (b) After 35 s, a carbon dimer in the GB are rotated perpendicular to the graphene plane. Magnified view of the flipping dimer is presented on top, along with the multislice simulated TEM image based on the atomic model in (g). (c) The dimer is eventually removed after another 22 s. (d–f) Maximum filtered images of (d–f). (g–i) Corresponding atomic models. The inset in (h) shows its side view. The scale bar in panel a is 1 nm.

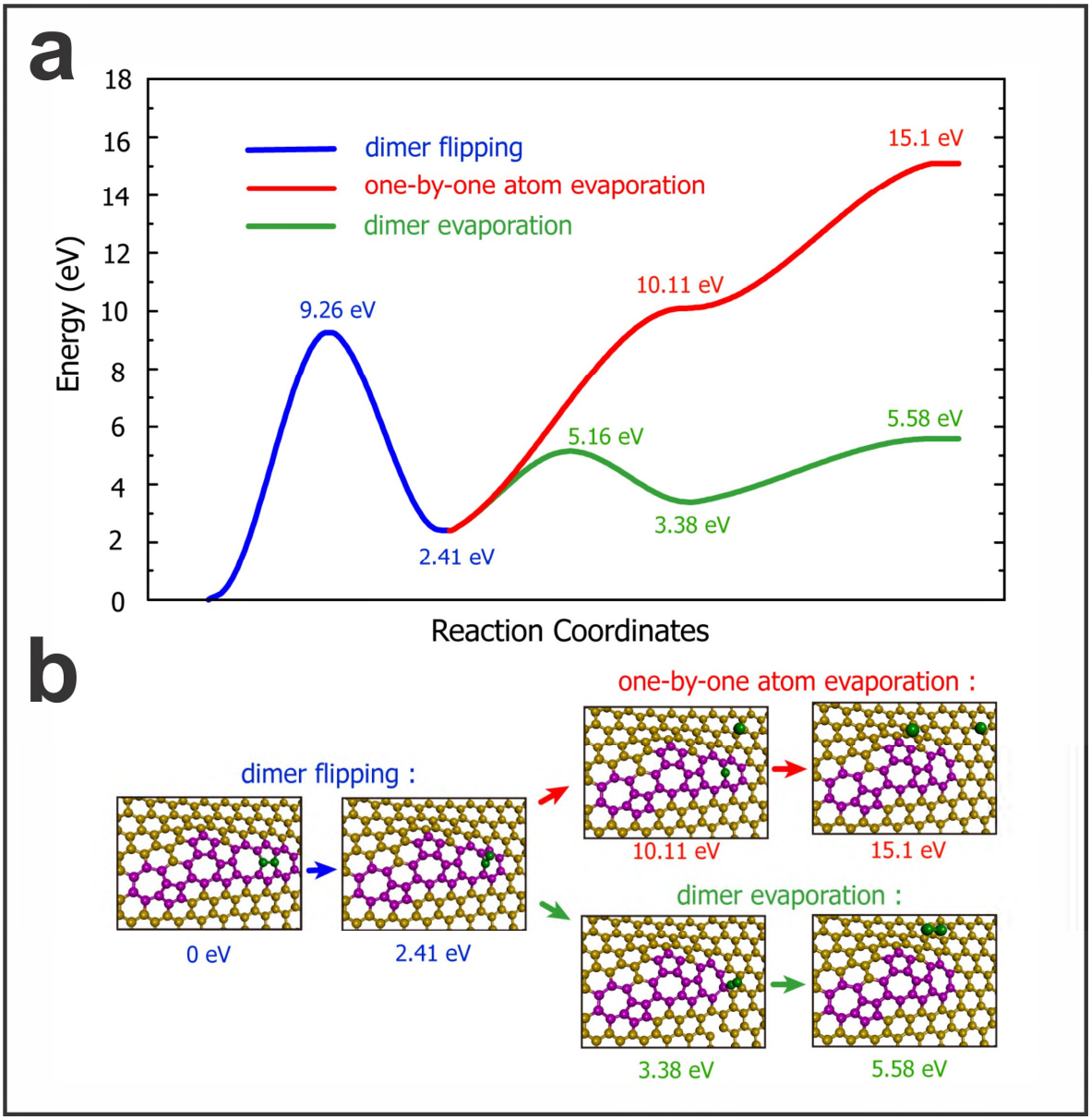

Figure 11. DFT calculated energy barriers of two mechanisms for the evaporation of a carbon dimer. (a) Energy curves for the dimer evaporation. In both pathways, the carbon dimer needs to first overcome a 9.26 eV barrier and get vertically stacked (blue curve). The energy barriers to subsequently sputter the dimer as a whole is 2.75 eV and 2.2 eV respectively (green curve). The two carbon atoms may also be removed one after another which requires a total energy of 12.69 eV (red curve). (b) Atomic models and DFT calculated relative energies for the moments of dimer evaporation.

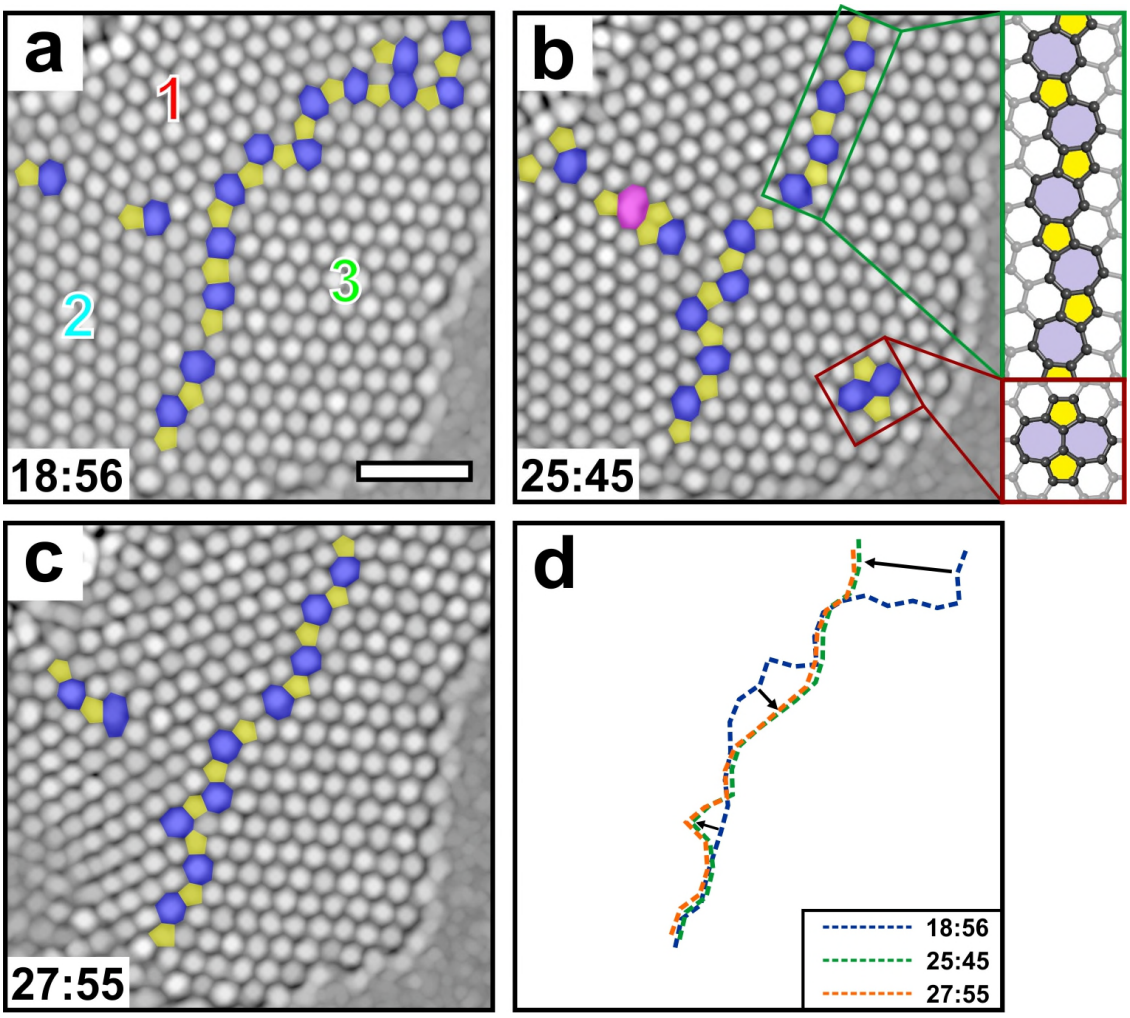

Figure 12. The stability of GBs. (a) Maximum filtered TEM images of the second layer graphene at 18 min 56 s. (b) The same area imaged after 6 min 49 s, with atomic models of the GB between Grain 1 and 3, and SW defect near the edge shown in the insets. (c) The same area imaged 2 min 10 s after (b). (d) Dashed lines showing the evolution of the high mismatch angle GB, which are drawn by connecting the central point of adjacent pentagons and heptagons at the boundary. The migration direction of the GB is indicated by black arrows. The scale bar in panel a is 1 nm.

Here, we discuss why the coalescence of grains is drastically reduced after 11 min. When the grain reaches a certain size, the GBs progressively evolve into a less meandering structure. As a consequence, there is no defect or edge nearby for the GB to interact with. The maximum energy an electron can impart to a carbon atom is ~19 eV in our imaging condition (80 kV accelerating voltage, 800 ^{o}C), which is not sufficient for a dislocation to make long distance motion.[52] Although a bond rotation could still be

activated at the GB under 80 kV electron irradiation, it is not energetically favorable since the GB has evolved to a relatively straight and symmetric shape (green inset in Figure 12(b)). The rotated bond is more likely to quickly restore in another electron collision. In addition, we discover that the stability of GBs is dependent on the misorientation angles. In Figure 12, we presented images of second layer graphene taken after 18 min 56 s. Full time sequential frames is shown in Figure S4. We observed in total 9 bond rotations and 4 atoms lost in or near the low-angle tilt boundary between grain 1 and 2 from 18 min 56 s to 27 min 55 s, while 8 bond rotations and only one dimer sputtering (shown in Figure 9) occurred in the high-angle GB. Considering the lengths of the GBs, it is apparent that the high-angle one possess higher stability in our imaging condition. This is consistent with the theory proposed by Liu *et al.*[56] As the dislocation density increases with the gain mismatch angle, the strain introduced by the dislocations partially cancels each other and the out-of-plane distortion caused by the GBs become smaller, which has been proven to be robust under electron irradiation.[28] It is worth noting that the top right part of the high-angle GB (Figure 12(a)) rotates from the edge to the inner side in the first 6 min 49 s (migration direction shown in Figure 12(d)), which further straighten the GB. Once it configured into a linear and symmetric shape in Figure 12(b), no structural change took place in the next 2 min 10 s. We also see the SW defect (red inset in Figure 12(b)) appeared 4 times at the edge of grain 3 during the same period (Figure S4), which has been experimentally confirmed to help alleviate the strain induced by the high-angle GB in ref [55] and enhance its stability.

Conclusion

We study the *in situ* high temperature growth of secondary layers of graphene using Au nanoparticles as seeds for heterogeneous nucleation within an AC-TEM. We find that graphene starts to nucleate around the Au nanoparticle and continues to grow in the area under electron irradiation. The mechanism for growth front propagation is found to be an alternant process of carbon cluster deposition and indentation filling. A detailed study of the edge reveals that the occasionally observed dark contrasted lines arise from back-folding of the second layer. The secondary layer of graphene starts as highly polycrystalline, but

further crystallized under the combined effect of beam irradiation and increased thermal energy. Large grains grow at the expense of smaller ones *via* multiple bond rotations occurring almost simultaneously. The coalescence of grains near the edge further involves the interaction between GB and edge. The merging of grains stops when the grain reached a certain size. Afterward the GB migration is dominated by single glide and climb motions of dislocations. This sheds lights on how nanoparticle impurities on the surface of graphene could seed multilayer regions during CVD growth of graphene.

Methods

Synthesis of graphene

Monolayer graphene was synthesized by atmospheric pressure chemical vapor deposition (CVD) method using a melted copper sheet as the catalytic as previously reported.[10,47] The high purity copper foil (Alfa Aesar, Puratonic 99.999% pure, 0.1 mm thick) of ~1 cm^2 were placed on the molybdenum piece of same size(Alfa Aesar, 99.95% pure, 0.1mm thick), which were both loaded into a 1 inch quartz tube in the CVD system. Molybdenum act as a stable wetting layer to prevent liquid copper from balling. 100 s.c.c.m. H_2/Ar (20% H_2 in Ar), 100 s.c.c.m. CH_4 (1% CH_4 in Ar) and 200 s.c.c.m. 100% Ar were flowed for 30 minutes. CH_4 flow was switched off before increasing hot−zone temperature to 1090 ^oC. Once the temperature reached 1090 ^oC, the quartz tube was moved from the room temperature zone to the center of heating zone and annealed for 30 minutes. The flow of H_2/Ar was then reduced to 80 s.c.c.m. and 10 s.c.c.m. of 1% CH_4 in Ar was added for 90 min for graphene growth. After growth, the quartz was removed from the heating zone for rapid cooling in the air with CH_4 off.

Transfer

A PMMA scaffold (8% wt in anisole, 495k molecular weight) was spin−coated onto the graphene sheet at 4700 rpm for 60 s and then baked at 180 ^oC for 90 s to solidify. Afterwards the sample was made up of a molybdenum/copper/graphene/PMMA stack. The copper layer were etched by floating the sample on the mixed solution of iron (III) chloride and hydrochloride, leaving a floating graphene−PMMA film on

the top after 48 h. The film was collected using a clean glass slide and transferred onto the surface of the DI water for 30 min wash away remaining iron (III) chloride. To further dissolve excess iron chloride, the sample was transferred onto a 10% hydrogen chloride solution for 5 min, before rinsed again in the DI water for 30 min. The film was then transferred onto a SiN TEM grid designed for *in-situ* Transmission Electron Microscopy in a heating holder (DENSsolutions single tilt 30° fitted with DENSsolutions High Temperature EM heater chip with a maximum operating temperature up to 800°C). The thin SiN membrane on the heating holder contained several windows (size 3 × 0.2 μm) produced using a Zeiss NVision SEM: FIB prior to graphene transfer. These windows were essential to enable HRTEM imaging of the graphene lattice without contrast from the SiN membrane. The grid was then cured at 350 ^{o}C for 12 h to burn out PMMA, leaving clean graphene.

Electron Microscopy

AC-TEM images were taken at an accelerating voltage of 80 kV, using Oxford's JEOL JEM-2200MCO field emission transmission electron microscope with a CEOS image corrector.[27] Data were recorded using a Gatan Ultrascan 4K×4K CCD camera with 1–2 s acquisition times and 2 pixel binning. TEM images were processed using Image J. Smoothing of images was achieved by using a Gaussian blur filter in Image J.

In situ Heating Holder

To perform variable-temperature experiments, we used a commercially available *in situ* heating holder from DENS Solutions (SH30-4M-FS). In the DENS Solutions holder, heating the sample was achieved by passing a current through a platinum resistive coil imbedded in the TEM chip (DENS Solutions DENS-C-30). The resistance of the platinum coil is monitored in a four-point configuration, and the temperature is calculated using the Callendar–Van Dusen equation (with calibration constants provided by the manufacturer).

Density Functional Theory (DFT) calculation

The DFT calculations are performed within the generalized gradient approximation of Perdew−Burke−Ernzerhof (PBE) functional using Vienna ab initio simulation package (VASP) code.[57,58] The basis set contains plane waves up to an energy cutoff of 400 eV. The unit cells are constructed with 200 carbon atoms. The unit cells are periodically repeated in the lateral direction and contain the vacuum region of 30 Å. We choose only one k point, the Γ point because the unit cell is enough large. When structural relaxations are performed, the structure is fully relaxed until the force on each atom is smaller than 0.02 eV/Å.

Tight-Binding Molecular Dynamics (TBMD) simulation

The TBMD simulations are performed using a modified environment-dependent tight-binding (EDTB) carbon potential,[59] which is modified from the original EDTB carbon potential to study carbon sp2 bond networks[60] and has been successfully applied to investigations of various defect structures in graphene and carbon nanotubes. The details of the TBMD simulation methods have been described in a previous publication.[61] The self-consistent calculations are performed by including a Hubbard-U term in the TB Hamiltonian to describe correctly the charge transfers in carbon atoms of dangling bonds and to prevent the unrealistic overestimation of charge transfers. The equations of motion of the atoms are solved by the fifth order predictor-corrector algorithm with a time step of 1.0 fs. In the case of TBMD simulation for the merging of two grains via three bond rotations shown in Figure 3 and Movie 1, the simulation unit cell contains 200 atoms. The simulation is started at a temperature of 4,000 K under the canonical control of temperature. The temperature is gradually increased to 4,800 K under linear temperature control to accelerate the dynamics so that structural reconstruction could be observed during the simulation time. In the case of TBMD simulation for evaporation of a carbon dimer in the GB shown in Figure 6 and Movie 2, the simulation unit cell contains 200 atoms. The simulation was started at a temperature of 4,000 K under the canonical control of temperature and gradually increased to 5,000 K. The velocity scaling method was also used to control the temperature.

Supporting Information Available*:* The Supporting Information is available free of charge on the ACS Publications website. TEM images showing the growth of second layer graphene at 600 ^{o}C; EDX characterization of nanocrystals; TEM images showing another example of grain coalescence; full sequencing TEM frames from 18 min 56 s to 27 min 55 s. TBMD movies (AVI) showing the merging of two grains via three bond rotations and the evaporation of a carbon dimer in the GB

Acknowledgements

J.H.W. thanks the support from the Royal Society. C.G. thanks the support from the Clarendon Fund. G.-D.L. acknowledges support from the Supercomputing Center/Korea Institute of Science and Technology Information with supercomputing resources (KSC-2015-C3-011) and from NRF grant (RIAM No. 2010-0012670). S.H thanks the support from Nano Material Technology Development Program (2012M3A7B4049888) through NRF-MSIP and Priority Research Center Program (2010-0020207) through NRF-MOE.

References

(1) Li, X.; Cai, W.; An, J.; Kim, S.; Nah, J.; Yang, D.; Piner, R.; Velamakanni, A.; Jung, I.; Tutuc, E.; et al. Large-Area Synthesis of High-Quality and Uniform Graphene Films on Copper Foils. *Science* **2009**, *324*, 1312–1314.

(2) Alemán, B.; Regan, W.; Aloni, S.; Altoe, V.; Alem, N.; Girit, C.; Geng, B.; Maserati, L.; Crommie, M.; Wang, F.; et al. Transfer-Free Batch Fabrication of Large-Area Suspended Graphene Membranes. *ACS Nano* **2010**, *4*, 4762–4768.

(3) Bhaviripudi, S.; Jia, X.; Dresselhaus, M. S.; Kong, J. Role of Kinetic Factors in Chemical Vapor Deposition Synthesis of Uniform Large Area Graphene Using Copper Catalyst. *Nano Lett.* **2010**, *10*, 4128–4133.

(4) Bae, S.; Kim, H.; Lee, Y.; Xu, X.; Park, J.-S.; Zheng, Y.; Balakrishnan, J.; Lei, T.; Kim, H. R.; Song, Y. Il; et al. Roll-to-Roll Production of 30-Inch Graphene Films for Transparent Electrodes. *Nat. Nanotechnol.* **2010**, *5*, 574–578.

(5) Li, X.; Magnuson, C. W.; Venugopal, A.; Tromp, R. M.; Hannon, J. B.; Vogel, E. M.; Colombo, L.; Ruoff, R. S. Large-Area Graphene Single Crystals Grown by Low-Pressure Chemical Vapor Deposition of Methane on Copper. *J. Am. Chem. Soc.* **2011**, *133*, 2816–2819.

(6) Mattevi, C.; Kim, H.; Chhowalla, M. A Review of Chemical Vapour Deposition of Graphene on Copper. *J. Mater. Chem.* **2011**, *21*, 3324–3334.

(7) Kim, H.; Mattevi, C.; Calvo, M. R.; Oberg, J. C.; Artiglia, L.; Agnoli, S.; Hirjibehedin, C. F.; Chhowalla, M.; Saiz, E. Activation Energy Paths for Graphene Nucleation and Growth on Cu. *ACS Nano* **2012**, *6*, 3614–3623.

(8) Yu, Q.; Jauregui, L. A.; Wu, W.; Colby, R.; Tian, J.; Su, Z.; Cao, H.; Liu, Z.; Pandey, D.; Wei, D.; et al. Control and Characterization of Individual Grains and Grain Boundaries in Graphene Grown by Chemical Vapour Deposition. *Nat. Mater.* **2011**, *10*, 443–449.

(9) Wu, W.; Jauregui, L. A.; Su, Z.; Liu, Z.; Bao, J.; Chen, Y. P.; Yu, Q. Growth of Single Crystal Graphene Arrays by Locally Controlling Nucleation on Polycrystalline Cu Using Chemical Vapor Deposition. *Adv. Mater.* **2011**, *23*, 4898–4903.

(10) Wu, Y. A.; Fan, Y.; Speller, S.; Creeth, G. L.; Sadowski, J. T.; He, K.; Robertson, A. W.; Allen, C. S.; Warner, J. H. Large Single Crystals of Graphene on Melted Copper Using Chemical Vapor Deposition. *ACS Nano* **2012**, *6*, 5010–5017.

(11) Hao, Y.; Bharathi, M. S.; Wang, L.; Liu, Y.; Chen, H.; Nie, S.; Wang, X.; Chou, H.; Tan, C.; Fallahazad, B.; et al. The Role of Surface Oxygen in the Growth of Large Single-Crystal Graphene on Copper. *Science* **2013**, *342*, 720–723.

(12) Geng, D.; Meng, L.; Chen, B.; Gao, E.; Yan, W.; Yan, H.; Luo, B.; Xu, J.; Wang, H.; Mao, Z.; et al. Controlled Growth of Single-Crystal Twelve-Pointed Graphene Grains on a Liquid Cu Surface. *Adv. Mater.* **2014**, *26*, 6423–6429.

(13) Grantab, R.; Shenoy, V. B.; Ruoff, R. S. Anomalous Strength Characteristics of Tilt Grain Boundaries in Graphene. *Science* **2010**, *330*, 946–948.

(14) Wei, Y.; Wu, J.; Yin, H.; Shi, X.; Yang, R.; Dresselhaus, M. The Nature of Strength Enhancement and Weakening by Pentagon–heptagon Defects in Graphene. *Nat. Mater.* **2012**, *11*, 759–763.

(15) Kotakoski, J.; Meyer, J. C. Mechanical Properties of Polycrystalline Graphene Based on a Realistic Atomistic Model. *Phys. Rev. B: Condens. Matter Mater. Phys.* **2012**, *85*, 195447.

(16) Rasool, H. I.; Ophus, C.; Zhang, Z.; Crommie, M. F.; Yakobson, B. I.; Zettl, A. Conserved Atomic Bonding Sequences and Strain Organization of Graphene Grain Boundaries. *Nano Lett.* **2014**, *14*, 7057–7063.

(17) Rasool, H. I.; Ophus, C.; Klug, W. S.; Zettl, A.; Gimzewski, J. K. Measurement of the Intrinsic Strength of Crystalline and Polycrystalline Graphene. *Nat. Commun.* **2013**, *4*, 2811.

(18) Lee, G.-H.; Cooper, R. C.; An, S. J.; Lee, S.; van der Zande, A.; Petrone, N.; Hammerberg, A. G.; Lee, C.; Crawford, B.; Oliver, W.; et al. High-Strength Chemical-Vapor-Deposited Graphene and Grain Boundaries. *Science* **2013**, *340*, 1073–1076.

(19) Yazyev, O. V; Louie, S. G. Electronic Transport in Polycrystalline Graphene. *Nat. Mater.* **2010**, *9*, 806–809.

(20) Tsen, A. W.; Brown, L.; Levendorf, M. P.; Ghahari, F.; Huang, P. Y.; Havener, R. W.; Ruiz-Vargas, C. S.; Muller, D. a; Kim, P.; Park, J. Tailoring Electrical Transport across Grain Boundaries in Polycrystalline Graphene. *Science* **2012**, *336*, 1143–1146.

(21) Yasaei, P.; Kumar, B.; Hantehzadeh, R.; Kayyalha, M.; Baskin, A.; Repnin, N.; Wang, C.; Klie, R. F.; Chen, Y. P.; Král, P.; et al. Chemical Sensing with Switchable Transport Channels in Graphene Grain Boundaries. *Nat. Commun.* **2014**, *5*, 4911.

(22) Hashimoto, A.; Suenaga, K.; Gloter, A.; Urita, K.; Iijima, S. Direct Evidence for Atomic Defects in Graphene Layers. *Nature* **2004**, *430*, 17–20.

(23) Jeong, B.; Ihm, J.; Lee, G.-D. Stability of Dislocation Defect with Two Pentagon-Heptagon Pairs in Graphene. *Phys. Rev. B* **2008**, *78*, 165403.

(24) Yazyev, O. V.; Louie, S. G. Topological Defects in Graphene: Dislocations and Grain Boundaries. *Phys. Rev. B* **2010**, *81*, 195420.

(25) Carlsson, J. M.; Ghiringhelli, L. M.; Fasolino, A. Theory and Hierarchical Calculations of the Structure and Energetics of [0001] Tilt Grain Boundaries in Graphene. *Phys. Rev. B: Condens. Matter Mater. Phys.* **2011**, *84*, 165423.

(26) Kim, K.; Lee, Z.; Regan, W.; Kisielowski, C.; Crommie, M. F.; Zettl, A. Grain Boundary Mapping in Polycrystalline Graphene. *ACS Nano* **2011**, *5*, 2142–2146.

(27) Warner, J. H.; Margine, E. R.; Mukai, M.; Robertson, A. W.; Giustino, F.; Kirkland, A. I. Dislocation-Driven Deformations in Graphene. *Science* **2012**, *337*, 209–212.

(28) Lehtinen, O.; Kurasch, S.; Krasheninnikov, a V; Kaiser, U. Atomic Scale Study of the Life Cycle of a Dislocation in Graphene from Birth to Annihilation. *Nat. Commun.* **2013**, *4*, 2098.

(29) Lee, G.-D.; Yoon, E.; Hwang, N.-M.; Wang, C.-Z.; Ho, K.-M. Formation and Development of Dislocation in Graphene. *Appl. Phys. Lett.* **2013**, *102*, 021603.

(30) Lee, G.-D.; Yoon, E.; Wang, C.-Z.; Ho, K.-M. Atomistic Processes of Grain Boundary Motion and Annihilation in Graphene. *J. Phys. Condens. Matter* **2013**, *25*, 155301.

(31) Warner, J. H.; Fan, Y.; Robertson, A. W.; He, K.; Yoon, E.; Lee, G.-D. Rippling Graphene at the Nanoscale through Dislocation Addition. *Nano Lett.* **2013**, *13*, 4937–4944.

(32) Zhang, Z.; Yang, Y.; Xu, F.; Wang, L.; Yakobson, B. I. Unraveling the Sinuous Grain Boundaries in Graphene. *Adv. Funct. Mater.* **2015**, *25*, 367–373.

(33) Albrecht, T. R.; Mizes, H. A.; Nogami, J.; Park, S.; Quate, C. F. Observation of Tilt Boundaries in Graphite by Scanning Tunneling Microscopy and Associated Multiple Tip Effects. *Appl. Phys. Lett.* **1988**, *52*, 362–364.

(34) Huang, P. Y.; Ruiz-Vargas, C. S.; van der Zande, A. M.; Whitney, W. S.; Levendorf, M. P.; Kevek, J. W.; Garg, S.; Alden, J. S.; Hustedt, C. J.; Zhu, Y.; et al. Grains and Grain Boundaries in Single-Layer Graphene Atomic Patchwork Quilts. *Nature* **2011**, *469*, 389–392.

(35) An, J.; Voelkl, E.; Suk, J. W.; Li, X.; Magnuson, C. W.; Fu, L.; Tiemeijer, P.; Bischoff, M.; Freitag, B.; Popova, E.; et al. Domain (Grain) Boundaries and Evidence of "Twinlike" Structures in Chemically Vapor Deposited Grown Graphene. *ACS Nano* **2011**, *5*, 2433–2439.

(36) Kurasch, S.; Kotakoski, J.; Lehtinen, O.; Skákalová, V.; Smet, J.; Krill, C. E.; Krasheninnikov, A. V; Kaiser, U. Atom-by-Atom Observation of Grain Boundary Migration in Graphene. *Nano Lett.* **2012**, *12*, 3168–3173.

(37) Yang, B.; Xu, H.; Lu, J.; Loh, K. P. Periodic Grain Boundaries Formed by Thermal Reconstruction of Polycrystalline Graphene Film. *J. Am. Chem. Soc.* **2014**, *136*, 12041–12046.

(38) Lahiri, J.; Lin, Y.; Bozkurt, P.; Oleynik, I. I.; Batzill, M. An Extended Defect in Graphene as a Metallic Wire. *Nat. Nanotechnol.* **2010**, *5*, 326–329.

(39) Kim, D.; Kim, Y.; Ihm, J.; Yoon, E.; Lee, G.-D. Atomic-Scale Mechanism of Grain Boundary Motion in Graphene. *Carbon* **2015**, *84*, 146–150.

(40) Westenfelder, B.; Meyer, J. C.; Biskupek, J.; Kurasch, S.; Scholz, F.; Krill, C. E.; Kaiser, U. Transformations of Carbon Adsorbates on Graphene Substrates under Extreme Heat. *Nano Lett.* **2011**, *11*, 5123–5127.

(41) Liu, Z.; Lin, Y.-C.; Lu, C.-C.; Yeh, C.-H.; Chiu, P.-W.; Iijima, S.; Suenaga, K. In Situ Observation of Step-Edge in-Plane Growth of Graphene in a STEM. *Nat. Commun.* **2014**, *5*, 4055.

(42) Frenken, G. C. D. and D. W. van B. and M. J. R. and J. W. M. Graphene Formation on Metal Surfaces Investigated by in-Situ Scanning Tunneling Microscopy. *New J. Phys.* **2012**, *14*, 53033.

(43) Günther, S.; Dänhardt, S.; Ehrensperger, M.; Zeller, P.; Schmitt, S.; Wintterlin, J. High-Temperature Scanning Tunneling Microscopy Study of the Ordering Transition of an Amorphous Carbon Layer into Graphene on Ruthenium(0001). *ACS Nano* **2013**, *7*, 154–164.

(44) Patera, L. L.; Africh, C.; Weatherup, R. S.; Blume, R.; Bhardwaj, S.; Castellarin-Cudia, C.; Knop-Gericke, A.; Schloegl, R.; Comelli, G.; Hofmann, S.; et al. In Situ Observations of the Atomistic Mechanisms of Ni Catalyzed Low Temperature Graphene Growth. *ACS Nano* **2013**, *7*, 7901–7912.

(45) Dong, G.; Frenken, J. W. M. Kinetics of Graphene Formation on Rh(111) Investigated by In Situ Scanning Tunneling Microscopy. *ACS Nano* **2013**, *7*, 7028–7033.

(46) Günther, S.; Dänhardt, S.; Wang, B.; Bocquet, M.-L.; Schmitt, S.; Wintterlin, J. Single Terrace Growth of Graphene on a Metal Surface. *Nano Lett.* **2011**, *11*, 1895–1900.

(47) Fan, Y.; He, K.; Tan, H.; Speller, S.; Warner, J. H. Crack-Free Growth and Transfer of Continuous Monolayer Graphene Grown on Melted Copper. *Chem. Mater.* **2014**, *26*, 4984–4991.

(48) He, K.; Robertson, A. W.; Fan, Y.; Allen, C. S.; Lin, Y.-C.; Suenaga, K.; Kirkland, A. I.; Warner, J. H. Temperature Dependence of the Reconstruction of Zigzag Edges in Graphene. *ACS Nano* **2015**, *9*, 4786–4795.

(49) Warner, J. H.; Lin, Y.-C.; He, K.; Koshino, M.; Suenaga, K. Stability and Spectroscopy of Single Nitrogen Dopants in Graphene at Elevated Temperatures. *ACS Nano* **2014**, *11*, 11806–11815.

(50) Liu, Z.; Suenaga, K.; Harris, P. J. F.; Iijima, S. Open and Closed Edges of Graphene Layers. *Phys. Rev. Lett.* **2009**, *102*.

(51) Meyer, J. C.; Geim, A. K.; Katsnelson, M. I.; Novoselov, K. S.; Booth, T. J.; Roth, S. The Structure of Suspended Graphene Sheets. *Nature* **2007**, *446*, 60–63.

(52) Gong, C.; Robertson, A. W.; He, K.; Lee, G.-D.; Yoon, E.; Allen, C. S.; Kirkland, A. I.; Warner, J. H. Thermally Induced Dynamics of Dislocations in Graphene at Atomic Resolution. *ACS Nano* **2015**, *9*, 10066–10075.

(53) Li, L.; Reich, S.; Robertson, J. Defect Energies of Graphite: Density-Functional Calculations. *Phys. Rev. B: Condens. Matter Mater. Phys.* **2005**, *72*, 184109.

(54) Kim, Y.; Ihm, J.; Yoon, E.; Lee, G.-D. Dynamics and Stability of Divacancy Defects in Graphene. *Phys. Rev. B* **2011**, *84*, 075445.

(55) Gong, C.; He, K.; Robertson, A. W.; Yoon, E.; Lee, G.-D.; Warner, J. H. Spatially Dependent Lattice Deformations for Dislocations at the Edges of Graphene. *ACS Nano* **2015**, *9*, 656–662.

(56) Liu, T. H.; Gajewski, G.; Pao, C. W.; Chang, C. C. Structure, Energy, and Structural Transformations of Graphene Grain Boundaries from Atomistic Simulations. *Carbon* **2011**, *49*, 2306–2317.

(57) Perdew, J.; Burke, K.; Ernzerhof, M. Generalized Gradient Approximation Made Simple. *Phys. Rev. Lett.* **1996**, *77*, 3865–3868.

(58) Kresse, G.; Furthmüller, J. Efficient Iterative Schemes for Ab Initio Total-Energy Calculations Using a Plane-Wave Basis Set. *Phys. Rev. B* **1996**, *54*, 11169–11186.

(59) Lee, G. Do; Wang, C. Z.; Yoon, E.; Hwang, N. M.; Ho, K. M. Vacancy Defects and the Formation of Local Haeckelite Structures in Graphene from Tight-Binding Molecular Dynamics. *Phys. Rev. B: Condens. Matter Mater. Phys.* **2006**, *74*.

(60) Lee, G.-D.; Wang, C. Z.; Yoon, E.; Hwang, N.-M.; Kim, D.-Y.; Ho, K. M. Diffusion, Coalescence, and Reconstruction of Vacancy Defects in Graphene Layers. *Phys. Rev. Lett.* **2005**, *95*, 205501.

(61) Tang, M. S.; Wang, C. Z.; Chan, C. T.; Ho, K. M. Environment-Dependent Tight-Binding Potential Model. *Phys. Rev. B* **1996**, *53*, 979–982.

TOC graphic